ADVANCED MATERIALS INTERFACES

www.advmatinterfaces.de

Tuning Chiral Nematic Pitch of Bioresourced Photonic Films via Coupling Organic Acid Hydrolysis

Zheng Cheng, Huilin Ye, Feng Cheng, Hongyan Li, Yi Ma, Qing Zhang, Avi Natan, Alolika Mukhopadhyay, Yucong Jiao, Ying Li, Yongmin Liu, and Hongli Zhu**

Controlling the iridescent photonic film generated by self-assembly of colorless cellulose nanocrystal (CNC) from the nanoscale to macroscale is challenging. This study combines experimental and computational approaches to systematically investigate the correlation between electrostatic interactions and chiral nematic structures. The chiral nematic order of the CNC colloidal is preserved in solid films after the evaporation of water. The cross-sections of the iridescent film show a clear left-handed helical arrangement of nanocrystals. The helical structure with the aid of acrylic acid exhibits longer organized patterns. This work reveals that compared to CNC prepared by pure sulfuric acid (zeta potential −37.1 mV), the CNC prepared using coupled mineral sulfuric and organic acrylic acid has a higher zeta potential (−67.2 mV), which induces the increase of helical pitch of the cholesteric nematic phase from 312 to 409 nm and a red shift of the iridescent film. Consequently, the tuning of reflected light wavelength lies in the variation of chiral nematic pitch inside the layered structure, which gives rise to different iridescent colors. The bioresourced photonic film is appealing to both academia and industry where optical and photonic components are essential.

1. Introduction

Cellulose nanocrystals (CNCs), one form of sustainable cellulosic nanosized building blocks, have gained broad interest in the field of multifunctional materials. CNCs can be prepared from cellulosic biomass through controlled acid hydrolysis.[1] These bioresourced and rigid rod-like crystalline components are 2–30 nm in width and hundreds of nanometers in length.[2] Typically, in the process of sulfuric acid hydrolysis, the amorphous regions of cellulose fibers are removed, and the crystalline regions of cellulose fibers are cleaved into nanocrystals.[3] Meanwhile, the negatively charged sulfate ester groups are introduced onto the CNCs surface.[4] This is an important step for the stabilization of aqueous colloidal suspensions of CNCs due to their electrostatic repulsion.[5] Interestingly, anisotropic whisker-like CNCs can spontaneously self-organize into chiral nematic (or cholesteric) liquid crystalline phases above a certain critical concentration.[6] Furthermore, the electrostatically charged CNCs organize along a direction, rotating slightly along the helicoidal axis layer by layer to form a left-handed helical structure.[7] This chiral nematic self-assembly behavior is usually influenced by many factors including pH, temperature, particle size, ionic strength, surface chemistry, etc.[8] Fundamentally speaking, the chiral structure of CNCs arises from the twist of cellulose nanocrystals.[9] One of the unique characteristics of CNCs is that the chiral nematic order in colloidal can be preserved in solid films after complete water evaporation. The CNC films exhibit the properties of a chiral photonic crystal with a strong circular dichroism (CD), behaving as a standard cholesteric Bragg reflector.[10]

The intriguing capability of CNCs to self-assemble into chiral nematic iridescent films with a helical structure and their photonic properties and applications have attracted increasing attention.[11] Many research efforts have been put on the control of their optical properties.[12] And, it has been proved that the color of CNC films can be tuned in the drying process of crystalline nanorod assemblies, which is in response to certain stimuli.[13] Various methods have been explored to enhance the color of CNC films, including the addition of electrolytes or polymers to the CNC suspension, ultrasonication treatment prior to drying, and varying the drying temperature.[14] In addition, some researchers have used external electric or magnetic fields to control the CNC orientation in suspensions and to tune the photonic properties of the films.[15] Frka-Petesic et al. demonstrated that using electric fields is an effective method to dynamically control the iridescence properties of concentrated CNCs in a polar solvent.[16] Meanwhile, the use of magnets (NdFeB) has been reported to facilitate chiral nematic alignment

Z. Cheng, Dr. H. Li, Y. Ma, Q. Zhang, A. Natan, A. Mukhopadhyay, Dr. Y. Jiao, Prof. Y. Liu, Prof. H. Zhu
Department of Mechanical and Industrial Engineering
Northeastern University
Boston, MA 02115, USA
E-mail: h.zhu@neu.edu

H. Ye, Prof. Y. Li
Department of Mechanical Engineering
University of Connecticut
Storrs, CT 06269, USA
E-mail: yingli@engr.uconn.edu

F. Cheng
Department of Electrical and Computer Engineering
Northeastern University
Boston, MA 02115, USA

The ORCID identification number(s) for the author(s) of this article can be found under https://doi.org/10.1002/admi.201802010.

DOI: 10.1002/admi.201802010

of CNCs in suspension and thus to control the photonic properties of cholesteric CNC films.[17] Lately, Vignolini and co-workers pointed out that the reflected color of CNC microfilms can be changed in response to relative humidity, and it can realize reversible real-time colorimetric response.[18] Moreover, the combination of superior physical properties and ease of functionalization along with the fascinating chiral nematic behavior of the CNCs free-standing films have led to a variety of promising discoveries toward attractive, functional materials.[19] The cholesteric liquid crystalline phase formed by CNCs has been used as a template to synthesize novel chiral materials for advanced optical applications.[11b,20] Most recently, Xu et al. reported that chiral photonic CNC films can be used for ultrasecure polarization-based encryption, which will pave the way to develop the next-generation advanced photonic devices.[21] Although some researchers have used different acid especially the mineral acid to obtain the CNCs,[22] to the best of our knowledge, so far no one has reported the direct use of the synergistic effect of mineral sulfuric acid coupling organic acid hydrolysis to tailor the chiral nematic structure of CNC iridescent films.

Herein, in this work, the CNC iridescent films with different pitches were demonstrated by tuning the electrostatic interaction through the concentration of acrylic acid as described by the following steps (**Scheme 1**). The native cellulose extracted from trees (Scheme 1a) was hydrolyzed by acid, and the amorphous regions of the cellulose microfibrils (Scheme 1b) were selectively removed, leaving crystalline nanorods (Scheme 1c) in the reaction solution. In this study, the CNCs with higher negative charges were prepared by using the synergistic effects of sulfuric acid and acrylic acid. Besides the sulfate ester groups from sulfuric acid, carboxyl groups were also introduced onto the CNCs surface by acrylic acid assisted hydrolysis (Scheme 1d). The negative charges on CNCs surface produce strong repulsive interactions among the nanocrystals, which are good for the uniform dispersion of CNCs and to form highly stable aqueous suspensions, thus affecting self-assembly of CNCs in the chiral nematic structure. Consequently, the higher zeta potential (absolute value) of CNCs prepared with coupled sulfuric acid and acrylic acid hydrolysis induces stronger electrostatic repulsion and thus promotes the formation of a larger helical pitch (Scheme 1e). After the slow evaporation of water, the chiral nematic structure is preserved in the solid film, as shown in Scheme 1f. The Bragg reflection shows an obvious red shift of the iridescent color in the solid SA-CNC (obtained by coupled sulfuric acid and acrylic acid) film compared to S-CNC (obtained by only sulfuric acid) film, which is determined by the chiral nematic structure featured with a larger helical pitch. The relation between the chiral nematic pitch of cellulose nanocrystal thin films and the surface charge was further studied by molecular dynamics (MD) simulations. The adjustment of charge groups on the CNC surface is an alternative path to tailor the chiral nematic structure of the CNC solid films. Our study is of great significance, because the tunable cholesteric color can be programmed as an interference device, with the capability to change the reflected circularly polarized light over a specific wavelength range. More importantly, affordable fabrication of bioresourced photonic film makes Bragg reflectors more readily available for sensors, optical filters, and the replacement for pigment-based coatings.

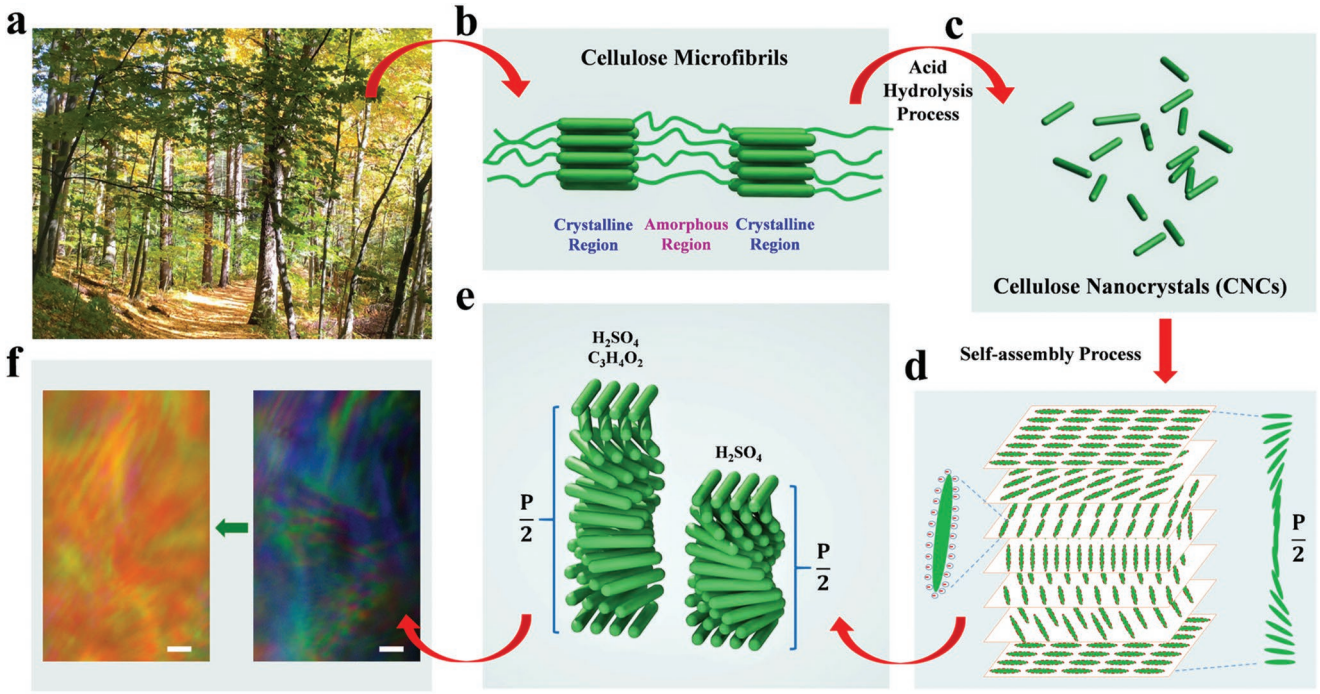

Scheme 1. Schematic illustration of the left-handed chiral nematic structured iridescent films formed by the chiral CNCs. a) Natural trees; b) Cellulose microfibrils composed of crystalline and amorphous regions; c) CNC nanorods were obtained after acid hydrolysis process; d) The self-assembly process of CNCs; e) A schematic diagram of the variation in half-helical pitch of CNCs derived from coupled sulfuric acid and acrylic acid hydrolysis compared to that derived from sulfuric acid hydrolysis, showing an obvious left-handed helical structure. "P" represents the helical pitch; f) A clear red shift of the iridescent color in the CNC films is observed with the polarized optical micrograph, (scale bar: 2 μm).

2. Result and Discussion

In this work, the CNCs were fabricated by using a combination of sulfuric acid and acrylic acid. The experimental methods section covers the experimental details. The mechanism of the incorporation of sulfate ester groups and carboxyl groups onto the surface of CNC with higher zeta potential (absolute value) is illustrated in **Figure 1**. The abundance of hydroxyl groups on the surface of cellulose chain (Figure 1a) leads to multiple chemical reactions producing a variety of cellulose derivatives with new functional groups.[23] Acid hydrolysis of cellulose involves rapid protonation of glucosidic oxygen by acid dissociation, and a subsequent slow splitting of glucosidic bonds induced by the water (Figure 1b).[24] Preserving the basic backbone structure, the hydrolysis process obtains two fragments with shorter chains.[25] Acrylic acid is an unsaturated organic acid which contains a carboxyl group and a vinyl group. Besides chain scission, hydrolyzing cellulose with acrylic acid also involves other reactions with the hydroxyl groups, such as esterification, grafting, and hydrogen bonding (Figure 1c).[5c,9] It is well known that sulfuric acid and carboxylic acid can esterify cellulose through Fischer esterification. Applying sulfuric acid to cellulose can result in semi-acid esters, and acrylic acid can form carboxylic esters containing vinyl groups.[26] More importantly, in the heating and concentrated acid environment, the exposed vinyl groups ($-CH=CH_2$) near or on the surface of CNC could act as initiators for the free radicals grafting of cellulose with unsaturated monomers, which contain carboxyl groups and can easily be converted to carboxylic acid. Allen et al. pointed out that cellulose derivatives containing carboxylic acid groups can be obtained by free-radical grafting of cellulose with unsaturated monomers (including acrylic acid, methacrylic acid, and their lower alkyl esters). They also claimed that cellulose can react with acrylic acid to make a cellulose derivative containing carboxyl group.[26a] In addition, Choi et al. have proved that acrylic acid can be bound to bacterial cellulose.[27] And the exposed vinyl groups on the surface of CNCs with radical centers can lead to the formation of multifunctional bonding sites and a collection of neighboring acrylic acid.[28] The acrylic acid located near the crystalline nanorod scaffold can undergo hydrogen bonding with the polar and sulfonated CNC surface. As a result, the presence of acrylic acid occupies some free volumes of CNC, resulting in steric stabilization.[29] In addition, physical adsorption of organic acid can also enhance the number of carboxyl groups on the surface of CNC.[30] In summary, the multiple reactions induced by the addition of acrylic acid result in more groups on the surface of CNC (Figure 1d), which induces the higher absolute surface zeta potential.

In order to investigate the quantitative relation between the zeta potential and chiral nematic pitch, acrylic acid of various

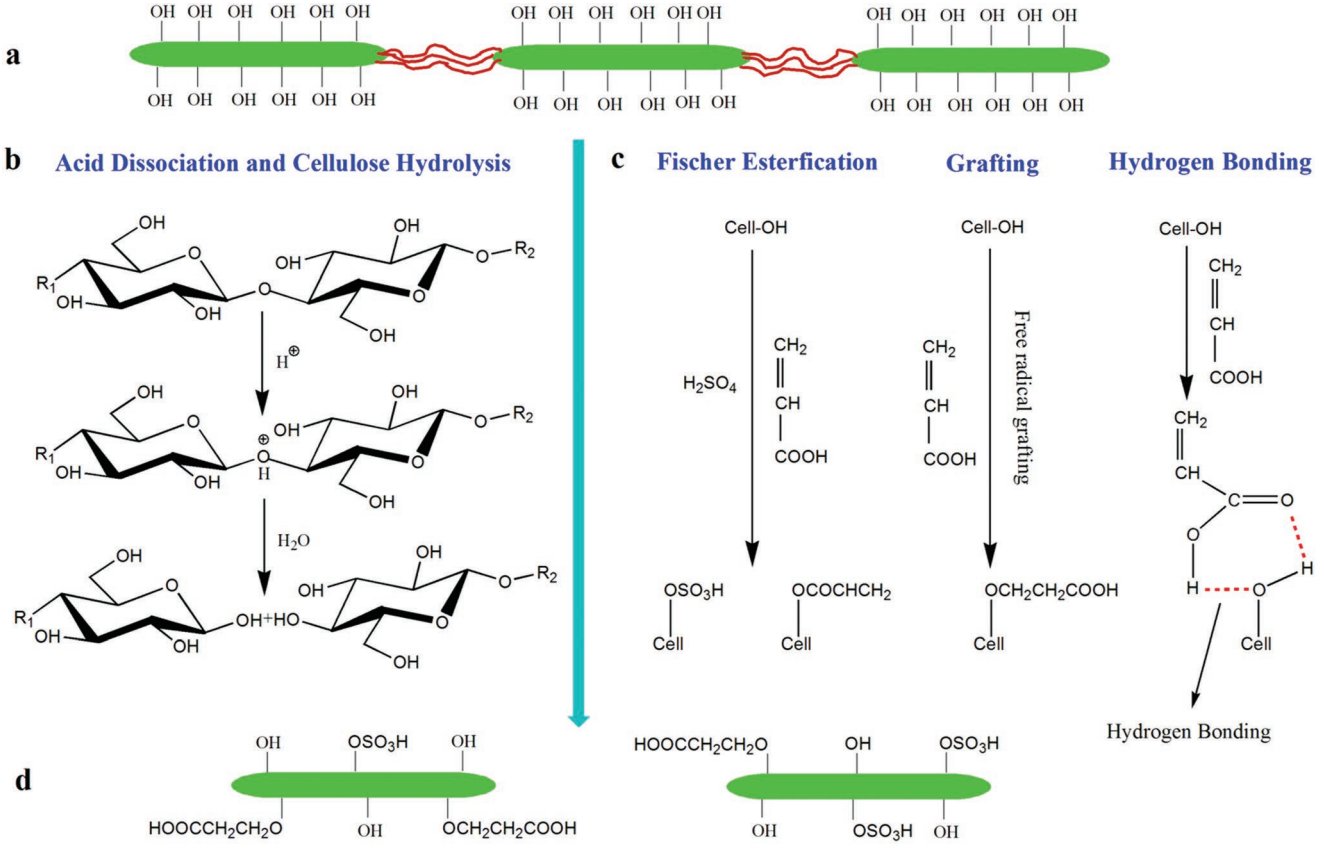

Figure 1. Mechanisms illustrating the simultaneous occurrence of cellulose hydrolysis and the correlated reaction of hydroxyl groups on the cellulose nanocrystals using a mixture of sulfuric acid and acrylic acid. a) The presence of hydroxyl groups on the surface of cellulose chain; b) Acid hydrolysis reaction, including acid dissociation and cellulose hydrolysis; c) Fischer esterification,[23c] grafting,[27] and hydrogen bonding are the main paths for incorporation of acrylic acid and CNC; d) Sulfate ester and carboxyl groups exposed on the CNC nanorods.

concentrations was dropped into the sulfuric acid solution. The concentrations of 0, 3, 5, 7, 10, and 15 mL are denoted as S-CNC, SA-3-CNC, SA-5-CNC, SA-7-CNC, SA-10-CNC, and SA-15-CNC, respectively. The final concentrations of sulfuric acid and acrylic acid in the reaction medium are shown in Table S1 in the Supporting Information. It can be seen that increasing the concentration of acrylic acid lowers the concentration of sulfuric acid. The SA-3-CNC, SA-5-CNC, and SA-7-CNC all have suitable strong acid concentration for producing CNC, which is ascribed to the fact that crystalline and noncrystalline cellulose regions have different resistance to acid attack.[31] Zeta potential measurements of the CNC suspensions were obtained to evaluate their surface charges. As the concentration of acrylic acid increases from 0 to 5 mL, the zeta potential (absolute value) increases from −37.1 to −67.2 mV. Beyond the concentration of 5 mL, the zeta potential decreases to −45.9 mV at the concentration of 15 mL, as shown in **Figure 2**a. The zeta potential of SA-5-CNC reaches the most negative value of −67.2 mV by the addition of 5 mL of acrylic acid. The initial increase in zeta potential with increased concentration of acrylic acid could be attributed to the increasing carboxyl groups. The following decrease above the concentration of 5 mL might be due to the dilution of sulfuric acid concentration by excess acrylic acid, which results in a drop of the acid hydrolysis process.

The UV–vis spectra of the series of CNC films containing different concentrations of acrylic acid are compared in Figure 2b, where the tunable reflection wavelengths are demonstrated. The peak wavelength of the minimum of transmitted light corresponding to the maximal reflection wavelength (λ_{max}), and λ_{max} can be tailored by altering P according to the Bragg reflection theory

$$\lambda_{max} = n_{avg} P \quad (1)$$

λ_{max}, n_{avg}, and P are the peak wavelength of reflected light, the average refraction index, and the helical pitch length, respectively.[20] For a chiral nematic structure, n_{avg} (1.54) is the same for CNC films. λ_{max} shifts from 480 nm for the film prepared with S-CNC to 630 nm for that prepared with SA-5-CNC. According to the Bragg reflection, the pitch increases from 312 to 409 nm. The shift of UV–vis spectrum corresponds to an increase in helical pitch length, and the iridescent color exhibits red shift. This is because the change in color arises from the shift in the pitch of the chiral nematic structure.[32]

The compositions and properties of the resulting CNCs are summarized in **Table 1**. The zeta potential (absolute value) increases first and then decreases, as the dosage of acrylic acid increases with the value ranging between −37.1 and −67.2 mV. It is worth noting that the chiral nematic pitch shows a consistent positive correlation with increasing zeta potential (Figure 2c). With increasing zeta potential from −37.1 to −67.2 mV, a continuous red shift of the predominant reflectance peaks from 480 to 630 nm due to an increase in the helical pitch was observed. Furthermore, the sulfate half-ester and carboxylic acid groups on CNCs were quantified by conductometric titration, and the typical titration curves for the S-CNC and SA-CNC samples are shown in Figure S1 (Supporting Information). The strong and weak acid groups (i.e., sulfate half-ester groups and carboxyl groups) can be discriminated from the curves.[33] It can be seen that the content of sulfate half-ester groups decreases from 0.20 to 0.13 mmol g^{-1} with the addition of acrylic acid from 0 to 15 mL, respectively. And the content of carboxyl groups first increases to 0.11 mmol g^{-1} and then decreases.

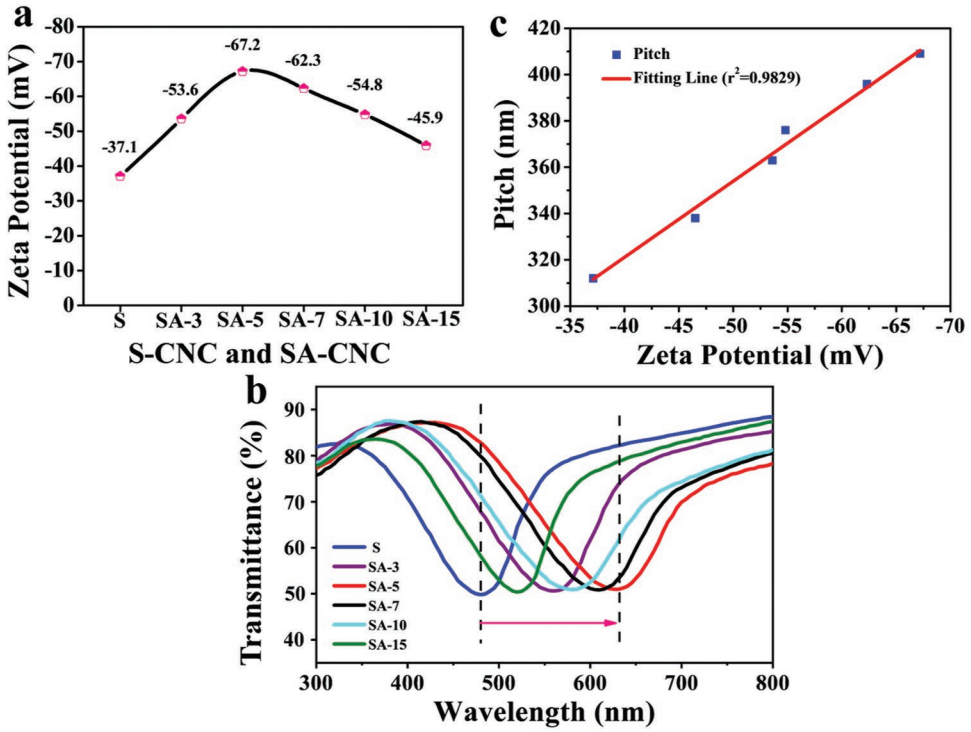

Figure 2. a) Zeta potential of S-CNC and SA-CNC suspension prepared with different amount of acrylic acid; b) UV–vis spectra of S-CNC and SA-CNC composite films; c) Correlation between the pitch and the zeta potential.

Table 1. Compositions and properties of CNCs.

Sample	Addition of acrylic acid [mL]	Zeta potential [mV])	$-SO_3H$ content [mmol g^{-1}]	$-COOH$ content [mmol g^{-1}]	Surface charge [mmol g^{-1}]	λ_{max} [nm]	P [nm]
S-CNC	0	−37.1 ± 0.5	0.20 ± 0.003	0	0.20 ± 0.003	480	312
SA-3-CNC	3	−53.6 ± 0.4	0.19 ± 0.004	0.07 ± 0.010	0.27 ± 0.005	560	363
SA-5-CNC	5	−67.2 ± 0.7	0.19 ± 0.006	0.10 ± 0.002	0.30 ± 0.008	630	409
SA-7-CNC	7	−62.3 ± 0.5	0.17 ± 0.005	0.10 ± 0.005	0.28 ± 0.005	610	396
SA-10-CNC	10	−54.8 ± 0.3	0.15 ± 0.003	0.11 ± 0.007	0.26 ± 0.007	580	376
SA-15-CNC	15	−45.9 ± 0.8	0.13 ± 0.009	0.11 ± 0.004	0.24 ± 0.006	520	338

It is obvious that the zeta potential has the consistent variation tendency with the total anionic surface charge (increasing first and then decreasing), and the highest zeta potential (−67.2 mV) also corresponds to the maximum anionic surface charge (0.30 mmol g^{-1}). Thus, it can be concluded that higher zeta potential leads to larger pitch of the chiral nematic structure in the solid CNC films and a red shift of the reflected color.

Since the sample SA-5-CNC has the highest zeta potential (absolute value) and the largest chiral nematic pitch, in the subsequent discussion, we focused on the sample of SA-5-CNC and denoted it as SA-CNC. Prior to the investigation of the film structure, the physical and chemical properties of the CNC suspension were studied. In order to exclude the size and size distribution of CNCs on the effect of the self-assembly process, transmission electron microscopy (TEM) images of the morphology for two kinds of as-prepared CNCs are shown in **Figure 3**a,b. Both kinds are found to form stable aqueous suspensions of rod-like cellulose particles.[34] The addition of acrylic acid to the CNC suspensions prepared with sulfuric acid makes no noticeable difference in the dimension or shape of the prepared S-CNCs. Dynamic light scattering (DLS) data shown in Figure S2 (Supporting Information) were used to prove this clarification. The morphologies of the two kinds of CNCs were profiled by atomic force microscopy (AFM) (Figure S3a,b, Supporting Information). It is apparent that the fine nanoparticles have uniform dispersion and no aggregation between individual nanocrystals. The uniform dispersion can be attributed to the negative charges on CNC, which prevents the aggregation and enhances stability. According to the AFM surface profile, a relatively narrow height distribution was observed, and the thickness of the SA-CNCs is in the range from 4 to 8 nm with no obvious difference from S-CNCs (Figure S4a,b, Supporting Information). With the addition of 5 mL acrylic acid, the zeta potential (absolute value) increases significantly to −67.2 mV, while the zeta potential without acrylic acid has a much lower zeta potential of −37.1 mV (Figure S5, Supporting Information). The high negative charges can be ascribed to the introduction of carboxyl groups from acrylic acid and the sulfate ester groups from sulfuric acid. It is concluded that the addition of acrylic acid contributes large amount of negative charges to CNCs, but has a negligible effect on CNC dimension.

Figure 3c,d shows the photographs of the prepared CNC suspension, which is placed between crossed polarizers. Both show shear optical birefringence features due to the light polarization by nematic orientation of the nanocrystals, which is considered to be the characteristic feature of an anisotropic liquid crystal. Such a birefringent pattern containing iridescent domains was formed due to negative charges on the surface of CNC. This confirms the absence of agglomeration as well as preservation of the self-assembly properties of CNC in suspension. The optical property of the CNC suspensions was further investigated by polarized optical microscopy (POM). The two kinds of CNC suspensions clearly show various disoriented iridescent color domains, including blue, green, yellow, and red. This is due to the random helical orientation of multidomain chiral nematic texture.[32b] Compared to S-CNC suspensions (Figure 3e), the SA-CNCs suspension (Figure 3f) exhibits more reddish and yellowish regions. In summary, with a rod-like shape, the S-CNCs and SA-CNCs are both well isolated from microcrystalline cellulose, and display self-assembly properties in water.

To further confirm the chemical structure, the Fourier transform infrared spectroscopy (FTIR) data were collected (**Figure 4**a). The representative spectrum of cellulose exhibits strong peaks at 3430–3500 and 1640 cm^{-1}, corresponding to −OH stretching and bending vibrations, respectively. The peak at 2900 cm^{-1} is associated with −CH stretching vibration. The peaks at 1430 and 1335 cm^{-1} correspond to the symmetric bending of $-CH_2$ and the bending vibration of −CH groups, respectively.[25] Besides the typical peaks from cellulose, there are extrinsic weak peaks at 1210 and 1230 cm^{-1}, owing to the stretching vibrations from −S=O groups. Meanwhile, the absorbance at 610 cm^{-1} is attributed to the −S−O stretching vibration.[35] The signature of −S=O and −S−O absorbance suggests that the sulfate ester group is successfully introduced by sulfuric acid hydrolysis. Additionally, the absorption band at 1720 cm^{-1} is assigned to −C=O stretching vibration, which proves the presence of carboxyl group from acrylic acid hydrolysis.[36] Therefore, it is evident that the acrylic acid contributed to the hydrolysis of cellulose and introduced carboxyl groups onto the surface of the cellulose. The crystallinity of CNCs was investigated using X-ray diffraction (XRD), as illustrated in Figure 4b. The CNCs obtained with or without the presence of acrylic acid both exhibit the typical peaks of $10\bar{1}$, 101, and 200, which are consistent with previous reports.[37] The measured crystallinity ratio of the CNC was 83% without acrylic acid and 85% with acrylic acid, which have a similar crystalline ratio within the error range. Chen et al. also proved that CNCs prepared with organic acid have small variation of crystalline ratio compared with those produced using mineral acids such as sulfuric acid.[23c]

Thermogravimetric (TGA) curves depict the thermal degradation of S-CNC and SA-CNC, as shown in Figure 4c. The

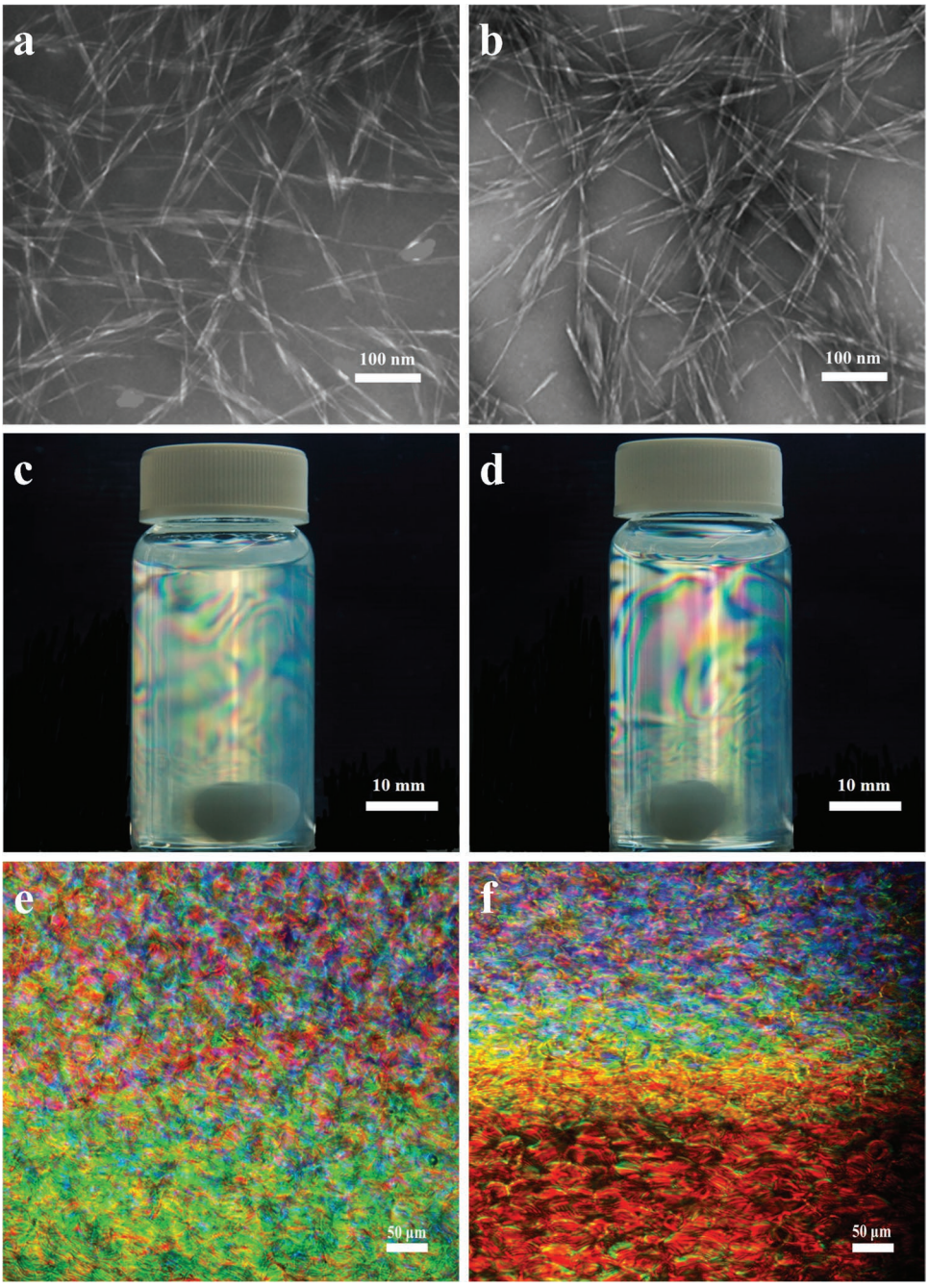

Figure 3. a) The TEM image of S-CNC; b) The TEM image of SA-CNC; c) S-CNC suspension (3.0 wt%) under stirring observed by crossed polarizers; d) SA-CNC suspension (3.0 wt%) under stirring observed by crossed polarizers; e) POM image of S-CNC suspension during evaporation; f) POM image of SA-CNC suspension during evaporation.

thermal stability of CNCs is also affected by the charged group originated from acrylic acid. The TGA curves of S-CNC and SA-CNC are distinguishable from each other because of their different thermal stabilities. The S-CNC shows the first stage of degradation temperature in the range of 160–185 °C. In comparison, the degradation temperature of SA-CNC is significantly higher and in the range of 190–216 °C, which is due to the use of less harsh acrylic acid.[38] Furthermore, the decomposition peak shifts from 185 to 216 °C, which is due to the presence of sulfate ester and carboxyl groups. Zhu et al. have proved that CNCs prepared with organic acid have better thermal stability than those produced with mineral acids such as sulfuric acid.[23c] Thereby, the addition of acrylic acid can significantly improve the corresponding thermal stability of the resultant CNCs. Intriguingly, phase separation can occur in certain concentrated suspensions of nanorod CNCs to form isotropic and chiral nematic liquid crystalline phases. CD can be used to measure the differences in apparent absorption of

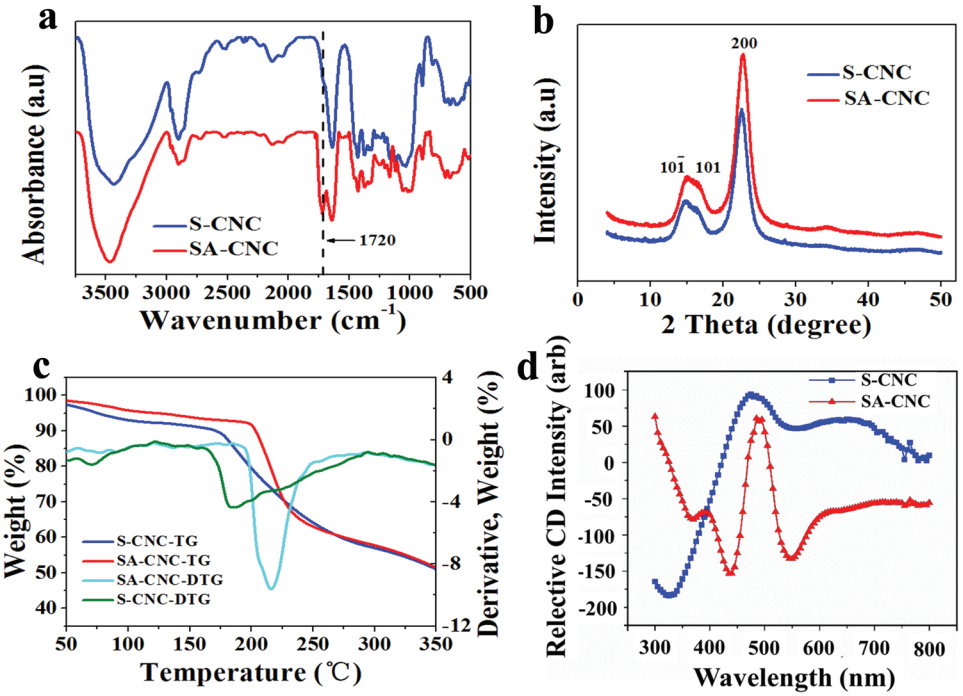

Figure 4. a) The FTIR pattern of cellulose nanocrystals; b) The XRD pattern of cellulose nanocrystals; c) The thermal stability property of cellulose nanocrystals; d) The circular dichroism spectra of cellulose nanocrystal films.

right- and left-handed circularly polarized light passing through chiral nematic liquid crystals. The sign of the CD is correlated with the handedness of the chiral nematic helical structure.[7b] It has been reported that the left-handed helical structure of CNCs gives rise to positive CD signals. The chiral nematic organized CNCs are responsive to the circular dichroism activity. Figure 4d shows the CD spectra of the SA-CNCs and S-CNCs films, both exhibiting a positive circular dichroism peak at about 500 nm, indicating the left-handed chiral nematic structure of CNCs.[6,39]

The well-ordered chiral nematic structure can be well preserved in the solid CNC film after complete water evaporation. **Figure 5**a,b shows a 44.5 µm thick film with the density of 1.28 g cm^{-3}. Compared to S-CNC films, the SA-CNC films display brighter iridescent color. As we have discussed, the helical pitch of CNCs with the addition of acrylic acid increases from 312 to 409 nm. The red shift of the reflection wavelength appeared as a result. Figure 5c,d shows the POM images of the surfaces of S-CNC and SA-CNC films. The obvious planar texture (spaced parallel lines) indicates that the organized helical structure is preserved in the solid films.[17] Compared to Figure 5e, the long-range ordered fingerprint pattern in Figure 5f is much clearer and neater. Also, the sample with larger pitch is redshift compared to the sample with a smaller pitch. This is in agreement with the observed spectra in Figure 2c. We thereby conclude that the color variation is associated with the variation of pitch inside the layered structure, and a larger pitch results in a longer reflected wavelength. The presence of carboxyl groups may contribute to the formation of organized patterns in iridescent films.

The chiral nematic structure of the CNC films fabricated with S-CNC and SA-CNC was further examined by scanning electron microscopy (SEM) (**Figure 6**a–d). The SEM images of the cross-section of the SA-CNC films give clear information of the film including the periodic layered structure, the pitch, and the orientation of the cellulose nanocrystals. Compared to the cross-section of S-CNC films (Figure 6a), the CNCs organized in the structure of the cross-section of SA-CNC films present a better periodic helix (Figure 6b). An organized layered structure was further identified in a higher magnification (50 k) in Figure 6c, and the long-range helical order can be observed. In addition, a twisting rod-like morphology is resolved and the organization of the cellulose crystal rods imitates a definite pattern. The periodic pattern is generally regarded as a half helical pitch with a 180° rotation angle.[40] The nanocrystals are oriented perpendicular to the fracture surface indicated by a yellow dotted circle, and have the tendency to be pulled out from fracture surface. The twisting occurs in a counter-clockwise direction (yellow arrow) when looking down the helical axis in the highest magnification (100 k), in agreement with a left-handed helical organization.[9,41] An interesting indication of a half-helical pitch is shown in Figure 6d. The half helical pitch (p/2) estimated from the cross-section of SEM images is similar to that calculated from the UV–vis spectrum. The presence of the periodic layered structure is evident throughout the entire thickness, and the chiral nematic order is uniform and well-defined.

It is well known that the boundary conditions of the twisted simulation cholesteric liquid crystals are difficult to handle, however several attempts have been made to model the CNC self-assembly.[42] To better understand the self-assembly mechanism of SA-CNC particles and further clarify the degree to which this could be modulated to tune the properties, MD simulations were conducted. The SA-CNC particles are modeled

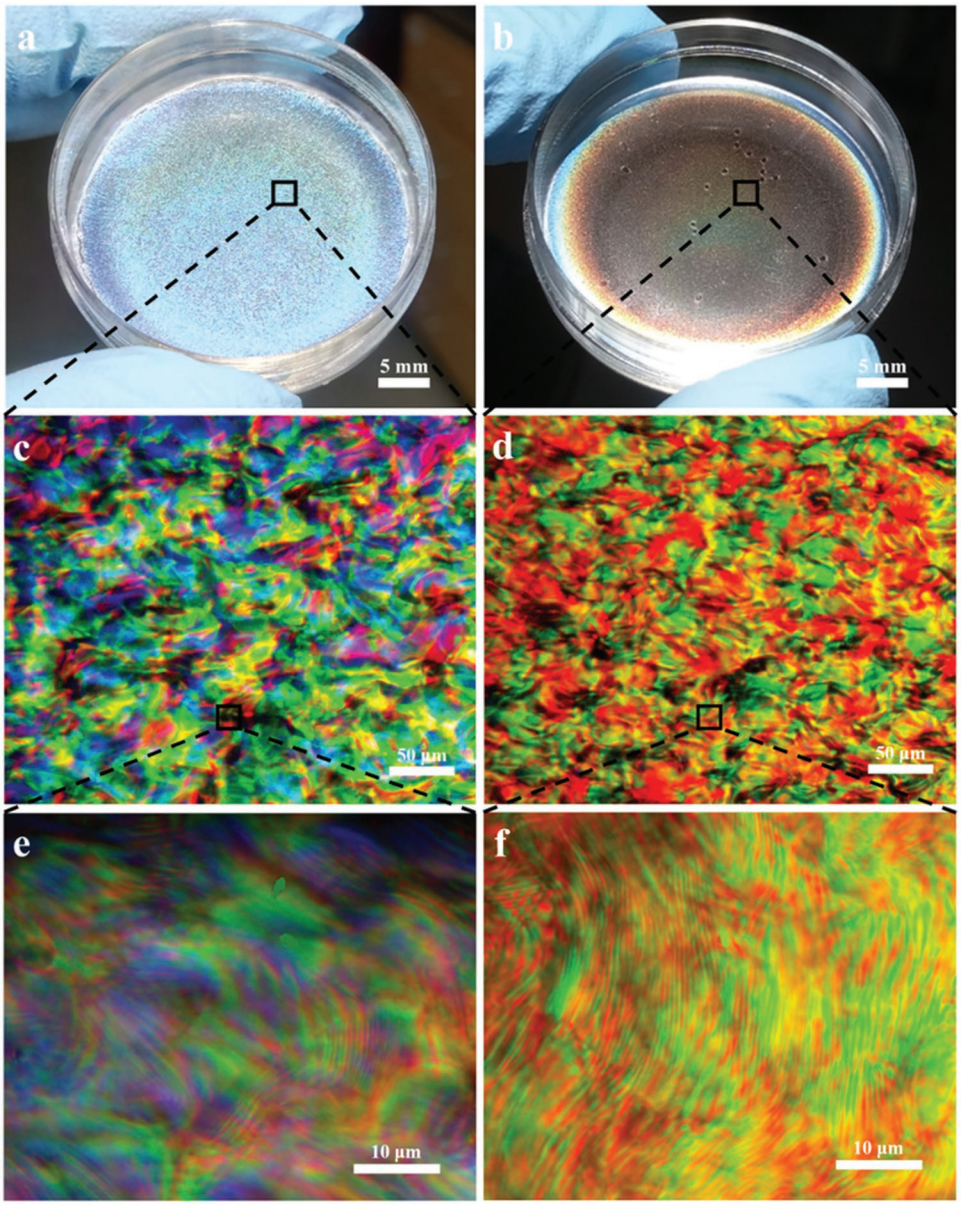

Figure 5. a,b) Photographs of S-CNC film and SA-CNC film; c,d) POM images of the surface of S-CNC film and SA-CNC film; e,f) Zoomed in POM images of the surface of S-CNC film and SA-CNC film.

as ellipsoidal molecules. The interactions between these ellipsoidal molecules are based on Gay–Berne (GB) potential,[43] which has been used extensively in simulations of liquid crystalline systems. The GB model is an anisotropic form of the Lennard–Jones 12–6 potential

$$U_{GB}\left(\vec{u}_i, \vec{u}_j, \vec{s}\right) = 4\varepsilon_0 \varepsilon^{\nu}\left(\vec{u}_i, \vec{u}_j, \vec{s}\right)\varepsilon'^{\mu}\left(\vec{u}_i, \vec{u}_j, \vec{s}\right) \left\{\left[\frac{\sigma_0}{r - \sigma\left(\vec{u}_i, \vec{u}_j, \vec{s}\right) + \sigma_0}\right]^{12} - \left[\frac{\sigma_0}{r - \sigma\left(\vec{u}_i, \vec{u}_j, \vec{s}\right) + \sigma_0}\right]^{6}\right\} \quad (2)$$

where $\sigma\left(\vec{u}_i, \vec{u}_j, \vec{s}\right)$, $\varepsilon^{\nu}\left(\vec{u}_i, \vec{u}_j, \vec{s}\right)$, and $\varepsilon'^{\mu}\left(\vec{u}_i, \vec{u}_j, \vec{s}\right)$ are anisotropic terms which are related to the shape and well-depth of liquid crystal, as described in detail in ref. [44]. $\vec{u}_i$ and $\vec{u}_j$ are the unit vectors that describe the orientation of the long axes of molecules i and j, respectively. $\vec{s}$ is defined as the interparticle unit vector, $\vec{s} = \vec{r}/r$, where $\vec{r} = \vec{r}_j - \vec{r}_i$, $r = |\vec{r}|$. $\vec{r}_i$ and $\vec{r}_j$ are the positions of molecules i and j, respectively. σ_0 and ε_0 are taken as units for distance and energy. The length-to-width ratio is $\kappa = \sigma_e/\sigma_s$, and side-by-side to end-to-end interaction strength ratio is $\kappa' = \varepsilon_s/\varepsilon_e$. Besides, an additive chiral interaction term is taken into account in order to consider the specific feature of chiral molecules. The chiral interaction is given by

$$U_c = 4\varepsilon_0 \varepsilon^{\nu}\left(\vec{u}_i, \vec{u}_j, \vec{s}\right)\varepsilon'^{\mu}\left(\vec{u}_i, \vec{u}_j, \vec{s}\right)\left[\frac{\sigma_0}{r - \sigma\left(\vec{u}_i, \vec{u}_j, \vec{s}\right) + \sigma_0}\right]^{7}\left[\left(\vec{u}_i \times \vec{u}_j\right)\cdot \vec{r}\right]\left(\vec{u}_i \cdot \vec{u}_j\right) \quad (3)$$

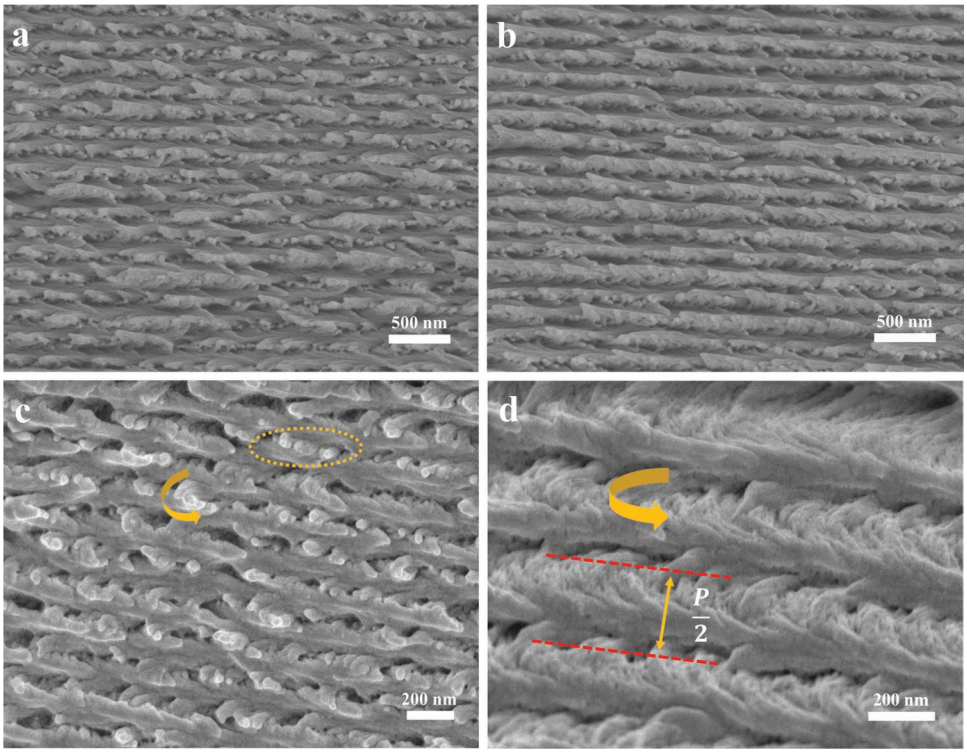

Figure 6. a) SEM images of the cross-section of S-CNC films (Magnification: × 20k); b–d) SEM images with different magnifications of the cross-section of SA-CNC films showing the clear helical structure (Magnification: b) × 20k; c) × 50k; d) × 100k). The yellow circle in (c) indicates examples of nanocrystal bundles pulled above fracture surface. The yellow arrow in (d) indicates a 180° counter-clockwise rotation of the director. The distance between two red dotted lines in (d) is a half helical pitch.

So the total energy for interparticle interaction is described as: $U = aU_{GB} + cU_c$. In this simulation, the molecules with parameters $\kappa = 3$, $\kappa' = 5$, $\mu = 1$ and $\nu = 2$ were confined in a rectangular box $L_x = L_y = 17$, $L_z = 51$ at constant number of molecules $N = 5184$ and temperature T, i.e., under the canonical ensemble NVT (N, V, and T represent number, volume, and temperature, respectively). The width of the molecule is 1 and corresponding to physical length is 6 nm. The scaled density of molecules is $\rho^* = \frac{N\sigma_0^3}{V} = 0.3$ and cutoff was set to $r^* = \frac{r}{\sigma_0} = 3.8$. We define chirality number as $c^* = \frac{c}{a}$, and chose it as 0.8. For all the MD simulations, the temperature was controlled at $T^* = k_B T/\varepsilon_0$. The surface charge strength was tuned by changing the repulsion energy unit ε_0 ranging from 0.1 to 0.3. Periodic boundary conditions were applied with all three directions for the simulation box.

Figure 7a shows snapshots of the self-assembly process of chiral nematic structures with three states for weak ($\varepsilon_0 = 0.1$) and strong ($\varepsilon_0 = 0.3$) surface charge repulsions-random (initial), transient(intermediate), and steady-state (final). The color of molecules represents the angle between principle long axes of molecules and their respective y-axis. It is found that, when there repulsion is weak, the randomly distributed structure gradually changes from quasi-regular to the steady regular structure with chiral nematic characteristics. Similarly, the chiral nematic is formed in the case of strong repulsion. However, the structures are not same for the following two cases. Figure 7b compares the side view of these two aforementioned structures. The pitch length is much smaller when weak repulsion is compared to the strong repulsion. The simulation box contained only half pitch structure for the enlarged pitch length of the chiral nematic structure, while the box was entirely filled with one pitch chiral structure for weak repulsion. To confirm that the structures found in our MD simulation are chiral nematic, the pseudoscalar radial orientational correlation function S_{221} was examined. This parameter is usually used to characterize helical superstructures and described as $S_{221} = -\sqrt{\frac{3}{10}}\left\langle\left[(\vec{u}_i \times \vec{u}_j)\cdot\vec{r}\right](\vec{u}_i \cdot \vec{u}_j)\right\rangle$, where brackets denote ensemble average. Figure 7c provides the value of S_{221} at intermolecular separation $r^* = 3.8$ as a function of the surface charge repulsion strength. According to the above definition, S_{221} should be zero for all intermolecular distances in the nematic phase, while nonzero for a chiral nematic phase at a short intermolecular distance. In particular, positive and negative values represent the left-handed and right-handed orientations, respectively. As shown in Figure 7c, nonzero S_{221} confirms the existence of chiral nematic structure in the MD simulations, and the S_{221} value increases with the increase of repulsion strength. The positive value of S_{221} in our simulations corresponds to the left-handed structure in experimental results. In addition, the pitch length of the chiral nematic structures was measured with different surface charge repulsions, as given in Figure 7d. The pitch length monotonically increases with the increment of repulsion from about 432 nm at $\varepsilon_0 = 0.1$ to 506 nm at $\varepsilon_0 = 0.3$. To some extent, this result is consistent with the experimental results. The minor discrepancy

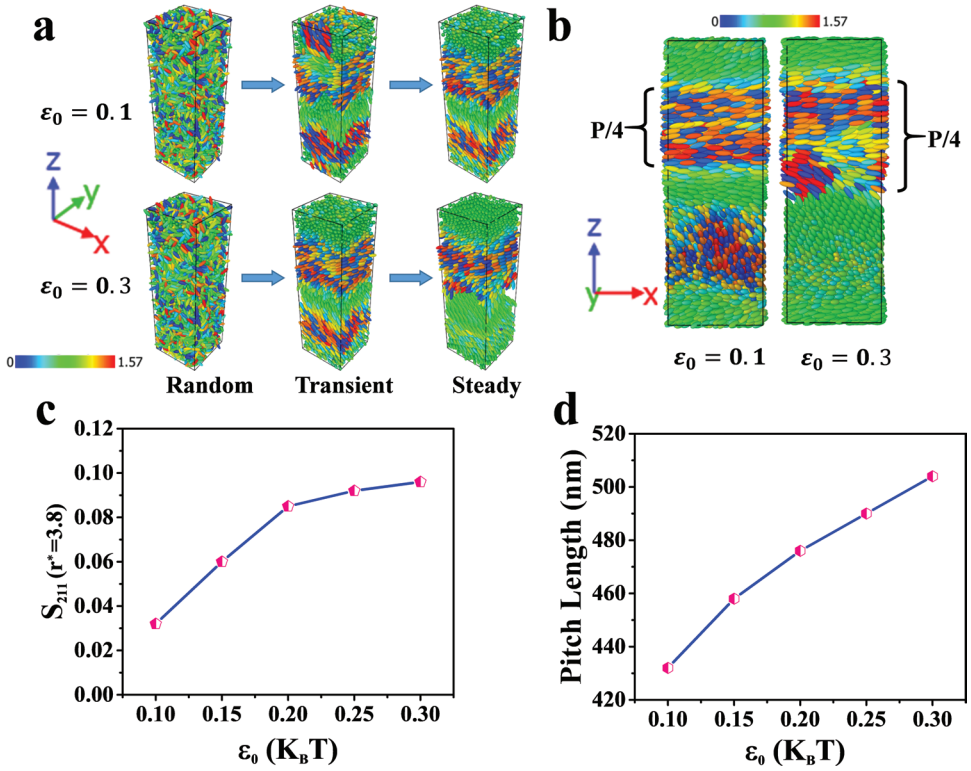

Figure 7. a) Snapshots showing self-assembly process of chiral nematic structure for CNC thin films with weak ($\varepsilon_0 = 0.1$) and strong ($\varepsilon_0 = 0.3$) surface charge repulsion; b) Side views to show the differences in pitch length between weak and strong repulsions; c) Pseudoscalar radial orientational as a function of repulsion strength; d) Pitch length as a function of repulsion strength. Color coded in (a) and (b) denotes the angle between the principle long axes of molecules and *y*-axis.

may be due to the use of 3 to 1 aspect ratio in MD simulations, whereas the relation between pitch length and surface charge repulsion strength is captured qualitatively in the experimental procedures. Therefore, it can be concluded from the MD simulation results that the surface charges on CNCs can be tuned to tailor the chiral nematic structure of CNC iridescent films, which is consistent with the experimental results.

3. Conclusions

In summary, for the first time, the CNCs with high negative charges were prepared via coupled mineral sulfuric acid and organic acrylic acid hydrolysis. The chiral nematic structure was well preserved in the solid film, and an obvious left-handed helical structure was observed. We found an agreement between the experimental and theoretical calculations, confirming the excellent positive correlation between the chiral nematic pitch and zeta potential. It was found that the CNCs formed a chiral nematic structure by electrostatic repulsion as a consequence of the negative surface charge. With the assistance of acrylic acid, the carboxyl groups were introduced onto the surface of the resultant CNC and the sulfate ester groups were also introduced from sulfuric acid. The high negative zeta potential (–67.2 mV) caused stronger electrostatic repulsion and promoted the formation of a larger helical pitch (409 nm) and the red shift of the iridescent color, which were confirmed by MD simulations. This study reveals that the electrostatic repulsion of CNC is the prevailing factor for affecting the iridescent color. The facile coupled organic acid hydrolysis to obtain CNCs can be a promising approach to tailor the chiral nematic structure.

4. Experimental Section

Materials: Microcrystalline cellulose and acrylic acid (99.5 wt%) were purchased from Sigma-Aldrich Co. Ltd. Sulfuric acid (95–98 wt%) for hydrolysis and regenerated cellulose dialysis tubes having a molecular weight cutoff of 12 000–14 000 were purchased from Fisher Scientific. All other chemicals used in these experiments were of analytical grade.

Sulfuric Acid Hydrolysis: CNCs were prepared by acid-catalyzed hydrolysis, as described below. 5 g of microcrystalline cellulose was added to 50 mL of 64.0 wt% sulfuric acid under constant mechanical stirring. Different dosages (3, 5, 7, 10, and 15 mL) of 99.5 wt% acrylic acid were then dropped into the solution. The hydrolysis was conducted at 50 °C and lasted for 50 min. The reaction was quenched by dilution with 10 times of the volume of water. The suspensions were washed with deionized water by repeated centrifuging. The supernatant was removed from the sediment and replaced with fresh deionized water and mixed. The centrifuge step was stopped until the supernatant became turbid. Subsequently, the resulting precipitate was dialyzed with deionized water for 20 days using regenerated cellulose dialysis membranes with a molecular weight cutoff of 12 000–14 000 until the pH of the water

remained constant. Finally, the dialyzed suspension was centrifuged with the CNC remained in the supernatant. The samples were sonicated in an ice bath to avoid overheating, which caused desulfation of the sulfate ester groups on the cellulose.

Film Casting/Preparation of Films: The 5 mL of 3.0 wt% CNC suspension was poured into a 35 mm diameter polystyrene petri dish (Manufactured from crystal-grade polystyrene for optical clarity. The surface is hydrophobic.) and allowed to evaporate at ambient conditions (30 °C, 80% RH) for 72 h. Then the films were peeled off from the petri dish for characterization. The S-CNC and SA-CNC films are both about 44.5 µm thick with a density of 1.28 g cm^{-3}.

FTIR: The 1.0 wt% CNCs suspension was deposited onto the KBr slice, and the FTIR spectra of the CNCs suspension were recorded using a Nicolet FTIR 5700 spectrophotometer (Bruker, Germany) in transmission mode over the range of 500 to 4000 cm^{-1} with a 4 cm^{-1} resolution at 25 °C.

Zeta Potential Test: Zeta potential was used to assess the surface charge and colloidal stability of the CNCs in suspension. Before the zeta potential test, the prepared CNC has been purified by being dialyzed against deionized water for 20 days in order to remove the residual sulfuric acid and acrylic until the pH of water remained constant. The zeta potential of 0.1 wt% aqueous CNC suspensions was measured at 25 °C without ionic strength adjustment using a zeta potential analyzer (HORIBA SZ-100, Japan). The reported zeta potential was averaged from the results of three measurements. The value obtained from the electrophoretic mobility for each sample following Smoluchowski model.

Determination of the Content of Sulfate Half-Ester Groups, Carboxyl Groups, and Total Surface Charge: The sulfate half-ester group content, carboxyl group content, and total anionic surface charge were measured by conductometric titration by following method of standard SCAN-CM 65:02 and previous literature.[30,33] Typically, 5 mL of 3.0 wt% CNC suspension was mixed with 80 g NaCl solution (1 mmol L^{-1}). The suspension was stirred and titrated with 0.05 mol L^{-1} NaOH in 0.1 mL increments, and the conductivity was recorded after each addition. The volume of consumed NaOH was obtained from the titration curve. Especially, the first equivalence point from titration is quantitatively related to the content of sulfate half-ester groups on the CNCs during acid hydrolysis. The value between first and second equivalence point gives the strong acid (—COOH) content. The surface charge of CNCs was calculated until all the negatively charged groups have been neutralized by NaOH. Each titration was performed in triplicate.

DLS: Dynamic light scattering was used to determine the hydrodynamic diameter of CNC suspensions using a particle size analyzer (HORIBA SZ-100, Japan). CNC suspensions were diluted to 0.01 wt% in advance. Each sample was replicated three times to obtain the averaged hydrodynamic diameter.

TEM: A small droplet of the diluted CNC suspension was deposited on a 300 mesh copper grid coated with carbon film. The excess liquid was absorbed by filter paper after 1 min. Subsequently, the samples were negatively stained with 1.5 wt% phosphotungstic acid for 1 min, blotted to remove excess liquid and dried at room temperature. Next, the TEM images were obtained by using a JEM-1010 transmission electron microscopy (JEOL, Japan) at an accelerating voltage of 80 kV.

AFM: The morphology of the CNCs was investigated using an atomic force microscopy (Parks XE7) (Bruker, Germany) employing the noncontact imaging mode. 10 µL of 0.001 wt% suspension was deposited onto a silica surface and air-dried.

CD Spectrum: Circular dichroism spectra were recorded on Jasco J-710 and Jasco J-810 spectrometers (JASCO Corporation, Japan). The films were mounted perpendicularly to the beam path. The acquisition conditions were as follows: data interval 12.0 nm, scan rate 100 nm min^{-1}, slit width 500 µm, and sensitivity 1000 mdeg. Mueller matrix transmission ellipsometry was performed in an RC2 spectroscopic ellipsometer. CD is defined as the difference in absorption of left- and right-handed circularly polarized light[45]

$$CD = A_L - A_f \quad (4)$$

where A_L is the absorption of left-handed circularly polarized light, and A_R is the absorption of right-handed circularly polarized light.

TGA: The thermal behavior of CNC samples was measured using SDTQ600 (TA Instruments, USA) under nitrogen atmosphere from room temperature to 400 °C at a heating rate of 10 °C min^{-1}.

XRD: X-ray diffraction tests were conducted on an X-ray diffractometer (UI tima IV, Japan) using Cu kα radiation at 40 kV and 30 mA. The scan is from a 2θ of 5° to 40° at a step size of 0.05°. The crystallinity ratio (CrI) was calculated from the following Equation (5)

$$CrI\ (\%) = (I_{002} - I_{am})/I_{002} \times 100 \quad (5)$$

For cellulose *I*, I_{002} is the diffraction intensity of the (002) crystal lattice plane and I_{am} is the diffraction intensity of $2\theta = 18°$.

POM: A home-built polarized optical microscopy was used to determine the cholesteric pitch of the liquid crystalline phase in the CNC films. The films were cut into pieces and placed directly on glass slides.

UV–Vis Spectrum: Light transmittance spectra of the films were measured from 300 to 800 nm with a TFProbe spectroscopic reflectometer (Agilent 8453, USA).

SEM: SEM (S3700 Hitachi Ltd. Japan) was used to examine the morphology of the liquid crystal films. The cross-section of the films was obtained by fracturing the sample in liquid nitrogen and then fixed it to a metal-base specimen holder using double-sided tape. The fixed samples were coated with a layer of ≈30 Å thick of gold or palladium. The accelerating voltage was 10 kV and the working distance was 11 mm.

Supporting Information

Supporting Information is available from the Wiley Online Library or from the author.

Acknowledgements

Z.C. and H.Y. contributed equally to this work. The authors acknowledge the financial support from Northeastern University. The work was also partially supported by the Department of Mechanical Engineering at the University of Connecticut. This research has benefited in part from the computational resources and staff contributions provided for the Booth Engineering Center for Advanced Technology (BECAT) at the University of Connecticut. The authors acknowledge the use of facilities from the Center for Nanoscale Systems (CNS) at Harvard University. H.Z. supervised and conceived this project. Z.C. corresponded the material preparation and characterization of the presented work. Z.C. conducted the experiments, collected and analyzed the data, and wrote the manuscript. F.C. and Y.M.L. conducted and analyzed part of the optical characterizations. H.Y. and Y.L. performed MD simulations on the self-assembly process of CNC thin films. All the authors contributed and commented on the manuscript.

Conflict of Interest

The authors declare no conflict of interest.

Keywords

cellulose nanocrystal, chiral nematic pitch, coupled organic acid, iridescent films, molecular dynamic simulation, self-assembly

Received: December 13, 2018
Revised: January 29, 2019
Published online:

[1] a) P. X. Wang, W. Y. Hamad, M. J. Maclachlan, *Nat. Commun.* **2016**, *7*, 11515; b) F. Jiang, A. R. Esker, M. Roman, *Langmuir* **2010**, *26*, 17919; c) J. F. Revol, L. Godbout, D. G. Gray, *J. Pulp Pap. Sci.* **1998**, *24*, 146.
[2] a) X. Xu, F. Liu, L. Jiang, J. Y. Zhu, D. Haagenson, D. P. Wiesenborn, *Appl. Mater. Interface* **2013**, *5*, 2999; b) B. L. Tardy, M. Ago, J. Guo, M. Borghei, T. Kämäräinen, O. J. Rojas, *Small* **2017**, *13*, 1702084.
[3] H. Zhu, W. Luo, P. N. Ciesielski, Z. Fang, J. Y. Zhu, G. Henriksson, M. E. Himmel, L. Hu, *Chem. Rev.* **2016**, *116*, 9305.
[4] X. M. Dong, J.-F. Revol, D. G. Gray, *Cellulose* **1998**, *5*, 19.
[5] a) H. Yu, Z. Qin, B. Liang, N. Liu, Z. Zhou, L. Chen, *J. Mater. Chem. A* **2013**, *1*, 3938; b) S. Camarero Espinosa, T. Kuhnt, E. J. Foster, C. Weder, *Biomacromolecules* **2013**, *14*, 1223; c) J. P. Lagerwall, C. Schütz, M. Salajkova, J. Noh, J. H. Park, G. Scalia, L. Bergström, *NPG Asia Mater.* **2014**, *6*, e80.
[6] A. Querejeta-Fernández, B. Kopera, K. S. Prado, A. Klinkova, M. Methot, G. Chauve, J. Bouchard, A. S. Helmy, E. Kumacheva, *ACS Nano* **2015**, *9*, 10377.
[7] a) J. Araki, S. Kuga, *Langmuir* **2001**, *17*, 4493; b) A. Querejeta-Fernández, G. g. Chauve, M. Methot, J. Bouchard, E. Kumacheva, *J. Am. Chem. Soc.* **2014**, *136*, 4788.
[8] a) T. Abitbol, D. Kam, Y. Levi-Kalisman, D. G. Gray, O. Shoseyov, *Langmuir* **2018**, *34*, 3925; b) W. Orts, L. Godbout, R. Marchessault, J.-F. Revol, *Macromolecules* **1998**, *31*, 5717.
[9] K. E. Shopsowitz, J. A. Kelly, W. Y. Hamad, M. J. Maclachlan, *Adv. Funct. Mater.* **2014**, *24*, 327.
[10] J. A. Kelly, M. Giese, K. E. Shopsowitz, W. Y. Hamad, M. J. Maclachlan, *Acc. Chem. Res.* **2014**, *47*, 1088.
[11] a) Y. Liu, D. Stoeckel, K. Gordeyeva, M. Agthe, C. Schutz, A. B. Fall, L. Bergström, *ACS Macro Lett.* **2018**, *7*, 172; b) K. E. Shopsowitz, W. Y. Hamad, M. J. MacLachlan, *Angew. Chem., Int. Ed.* **2011**, *50*, 10991.
[12] T. D. Nguyen, W. Y. Hamad, M. J. Maclachlan, *Chem. Commun.* **2013**, *49*, 11296.
[13] Y.-D. He, Z.-L. Zhang, J. Xue, X.-H. Wang, F. Song, X.-L. Wang, L.-L. Zhu, Y.-Z. Wang, *ACS Appl. Mater. Interfaces* **2018**, *10*, 5805.
[14] a) J. Pan, W. Hamad, S. K. Straus, *Macromolecules* **2010**, *43*, 3851; b) F. Azzam, L. Heux, B. Jean, *Langmuir* **2016**, *32*, 4305.
[15] a) K. J. De France, K. G. Yager, T. Hoare, E. D. Cranston, *Langmuir* **2016**, *32*, 7564; b) K. Fleming, D. Gray, S. Prasannan, S. Matthews, *J. Am. Chem. Soc.* **2000**, *122*, 5224.
[16] B. Frka-Petesic, H. Radavidson, B. Jean, L. Heux, *Adv. Mater.* **2017**, *29*, 1606208.
[17] B. Frka-Petesic, G. Guidetti, G. Kamita, S. Vignolini, *Adv. Mater.* **2017**, *29*, 1701469.
[18] T. H. Zhao, R. M. Parker, C. A. Williams, K. T. Lim, B. Frka-Petesic, S. Vignolini, *Adv. Funct. Mater.* **2018**, *12*, 1804531.
[19] K. E. Shopsowitz, W. Y. Hamad, M. J. MacLachlan, *J. Am. Chem. Soc.* **2012**, *134*, 867.
[20] K. E. Shopsowitz, H. Qi, W. Y. Hamad, M. J. MacLachlan, *Nature* **2010**, *468*, 422.
[21] H. Zheng, W. Li, W. Li, X. Wang, Z. Tang, S. X. A. Zhang, Y. Xu, *Adv. Mater.* **2018**, *30*, 1705948.
[22] O. M. Vanderfleet, D. A. Osorio, E. D. Cranston, *Philos. Trans. R. Soc., A* **2018**, *376*, 20170041.
[23] a) R. M. Parker, G. Guidetti, C. A. Williams, T. Zhao, A. Narkevicius, S. Vignolini, B. Frkapetesic, *Adv. Mater.* **2018**, *30*, 1704477; b) K. K. Sadasivuni, A. Kafy, L. Zhai, H. U. Ko, S. Mun, J. Kim, *Small* **2015**, *11*, 994; c) L. Chen, J. Zhu, C. Baez, P. Kitin, T. Elder, *Green Chem.* **2016**, *18*, 3835.
[24] B. Braun, J. R. Dorgan, *Biomacromolecules* **2009**, *10*, 334.
[25] P. Lu, Y. L. Hsieh, *Carbohydr. Polym.* **2010**, *82*, 329.
[26] a) T. C. Allen, J. A. Cuculo, *J. Polym. Sci., Part D: Macromol. Rev.* **1973**, *7*, 189; b) S. Spinella, A. Maiorana, Q. Qian, N. J. Dawson, V. Hepworth, S. A. McCallum, M. Ganesh, K. D. Singer, R. A. Gross, *ACS Sustainable Chem. Eng.* **2016**, *4*, 1538.
[27] Y. J. Choi, Y. Ahn, M. S. Kang, H. K. Jun, I. S. Kim, S. H. Moon, *J. Chem. Technol. Biotechnol.* **2004**, *79*, 79.
[28] J. Yang, C. R. Han, J. F. Duan, M. G. Ma, X. M. Zhang, F. Xu, R. C. Sun, X. M. Xie, *J. Mater. Chem.* **2012**, *22*, 22467.
[29] R. Bardet, N. Belgacem, J. Bras, *ACS Appl. Mater. Interfaces* **2015**, *7*, 4010.
[30] K. Rodríguez, S. Renneckar, P. Gatenholm, *ACS Appl. Mater. Interfaces* **2011**, *3*, 681.
[31] a) L. Chen, Q. Wang, K. Hirth, C. Baez, U. P. Agarwal, J. Zhu, *Cellulose* **2015**, *22*, 1753; b) Q. Wang, X. Zhao, J. Zhu, *Ind. Eng. Chem. Res.* **2014**, *53*, 11007.
[32] a) T.-D. Nguyen, W. Y. Hamad, M. J. MacLachlan, *Chem. Commun.* **2013**, *49*, 11296; b) K. Yao, Q. Meng, V. Bulone, Q. Zhou, *Adv. Mater.* **2017**, *29*, 1701323.
[33] S. Beck, M. Méthot, J. Bouchard, *Cellulose* **2015**, *22*, 101.
[34] Y. Tang, S. Yang, N. Zhang, J. Zhang, *Cellu* **2014**, *21*, 335.
[35] C. Z. Li, W. Qian, Z. K. Zhao, *Green Chem.* **2008**, *10*, 177.
[36] S. Fujisawa, Y. Okita, H. Fukuzumi, *Carbohydr. Polym.* **2011**, *84*, 579.
[37] a) J. Gong, J. Li, J. Xu, Z. Xiang, L. Mo, *RSC Adv.* **2017**, *7*, 33486; b) Y. Hu, N. Abidi, *Langmuir* **2016**, *32*, 9863.
[38] H. Qiao, Y. Zhou, F. Yu, E. Wang, Y. Min, Q. Huang, L. Pang, T. Ma, *Chemosphere* **2015**, *141*, 297.
[39] D. Qu, J. Zhang, G. Chu, H. Jiang, C. Wu, Y. Xu, *J. Mater. Chem. C* **2016**, *4*, 1764.
[40] A. G. m. Dumanli, H. M. van der Kooij, G. Kamita, E. Reisner, J. J. Baumberg, U. Steiner, S. Vignolini, *ACS Appl. Mater. Interfaces* **2014**, *6*, 12302.
[41] M. Giese, L. K. Blusch, M. K. Khan, M. J. Maclachlan, *Angew. Chem.* **2015**, *54*, 2888.
[42] a) A. Kuhnhold, T. Schilling, *J. Chem. Phys.* **2016**, *145*, 194904; b) C. Honorato-Rios, A. Kuhnhold, J. R. Bruckner, R. Dannert, T. Schilling, J. P. Lagerwall, *Front. Mater.* **2016**, *3*, 21.
[43] J. G. Gay, B. J. Berne, *J. Chem. Phys.* **1981**, *74*, 3316.
[44] R. Memmer, *Liq. Cryst.* **2000**, *27*, 533.
[45] O. V. Surov, M. I. Voronova, A. G. Zakharov, *Russ. Chem. Rev.* **2017**, *86*, 907.